Supplementary information

An Effective Sulfur Conversion Catalyst based on $MnCo_2O_{4.5}$ Modified Graphitized Carbon Nitride Nanosheet for High-Performance Li-S batteries

Wenhao Sun[a], Yi-Chun Lu[b,*],Yaqin Huang[a,*]

a. *Beijing Key Laboratory of Electrochemical Process and Technology for Materials, Key Laboratory of Biomedical Materials of Natural Macromolecules, Ministry of Education, Beijing University of Chemical Technology, Beijing 100029, People's Republic of China. *E-mail: huangyq@mail.buct.edu.cn*

b. *Electrochemical Energy and Interfaces Laboratory, Department of Mechanical and Automation Engineering, The Chinese University of Hong Kong, Shatin, New Territories 999077, Hong Kong SAR, People's Republic of China, *E-mail: yichunlu@mae.cuhk.edu.hk*

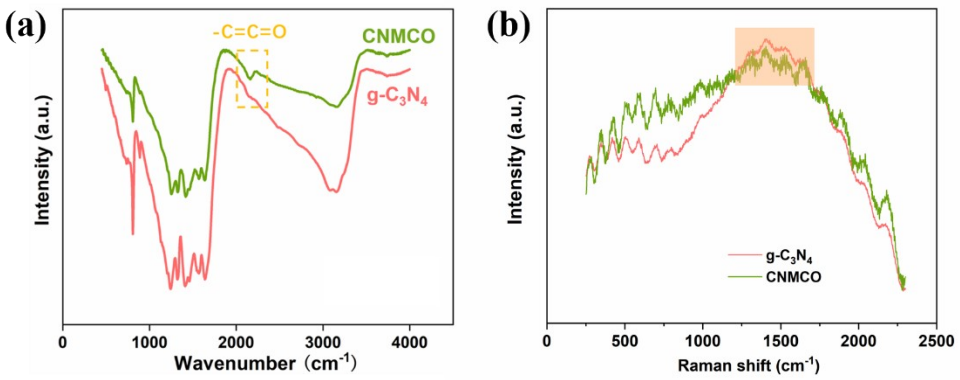

Figure S1. (a) FTIR spectra of g-C_3N_4 and CNMCO; (b) Normalized Raman spectra of g-C_3N_4 and CNMCO.

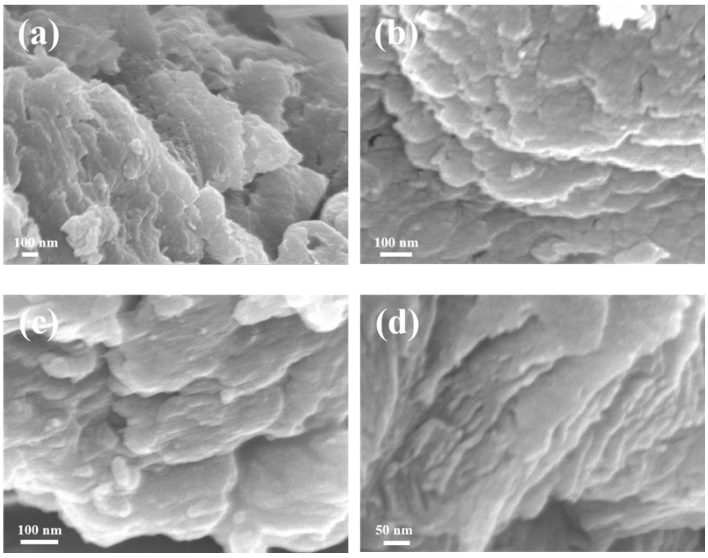

Figure S2. SEM images of g-C_3N_4.

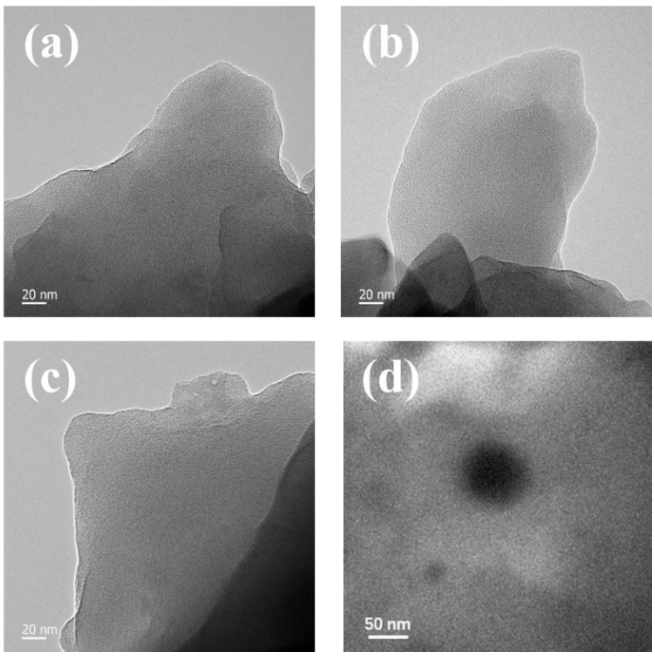

Figure S3. TEM images of (a-c) g-C_3N_4 and (d) $MnCo_2O_{4.5}$.

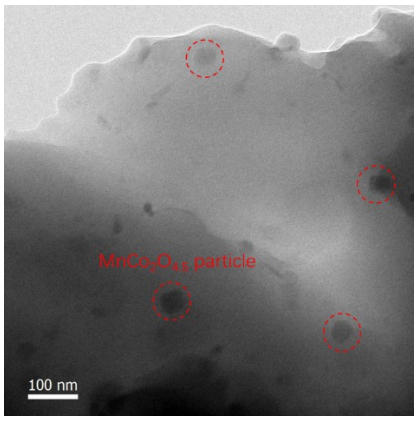

Figure S4. TEM image of CNMCO.

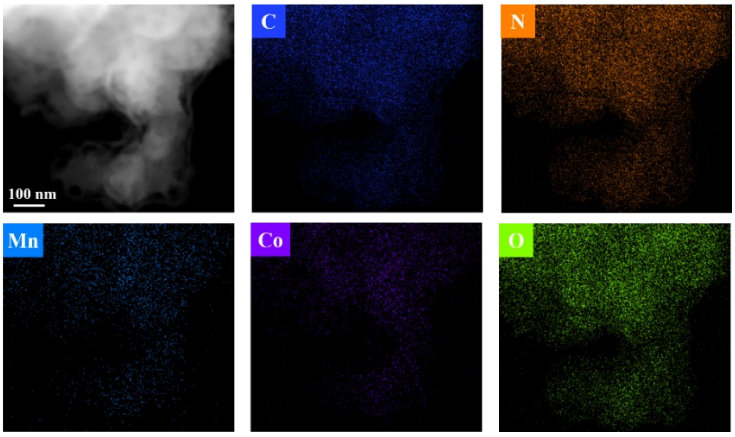

Figure S5. Elemental mapping images of C, N, Mn, Co and O in CNMCO.

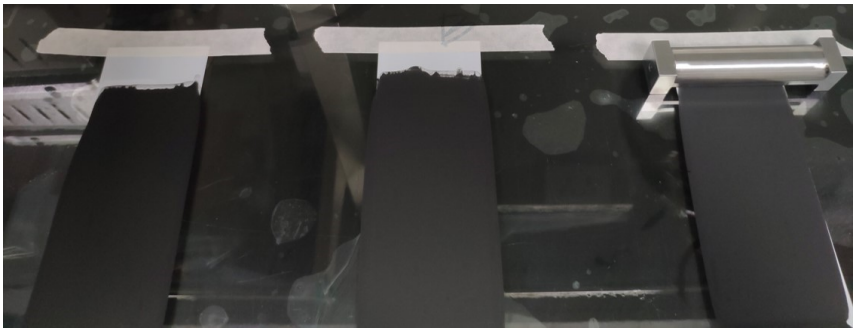

Figure S6. Photograph of the typical coating process for preparing CNMCO/PP separator.

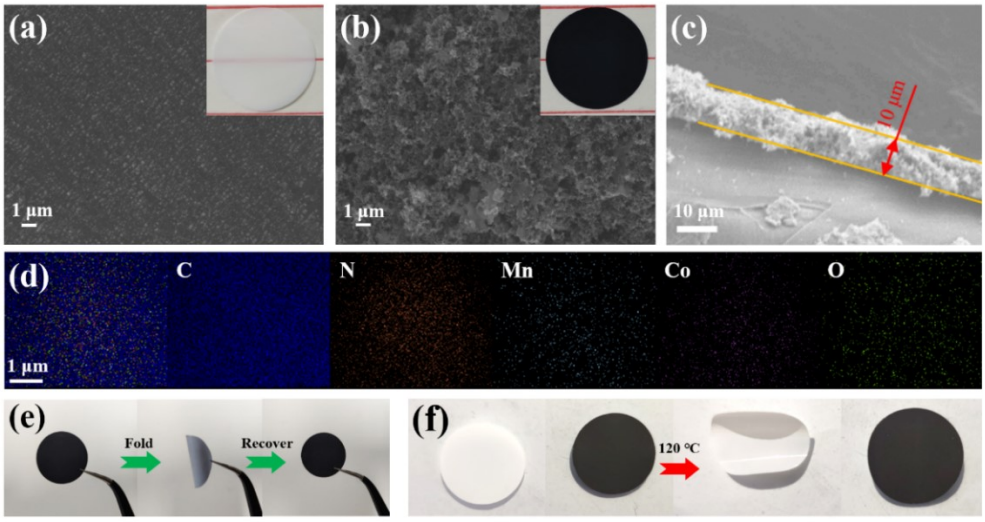

Figure S7. SEM images of (a) PP separator and (b) CNMCO/PP separator. (c) Cross-sectional SEM image of CNMCO/PP separator. (d) Elemental mapping images of C, N, Mn, Co and O in CNMCO/PP separator. (e) Demonstration of the mechanical stability of CNMCO/PP separator. (f) Digital images of PP separator and CNMCO/PP separator before and after thermal treatment at 120 °C for 5 min.

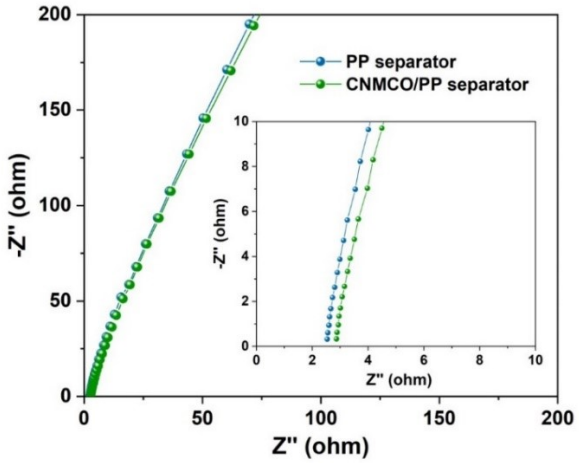

Figure S8. EIS plots of PP separator and CNMCO/PP separator sandwiched between the stainless steel electrodes.

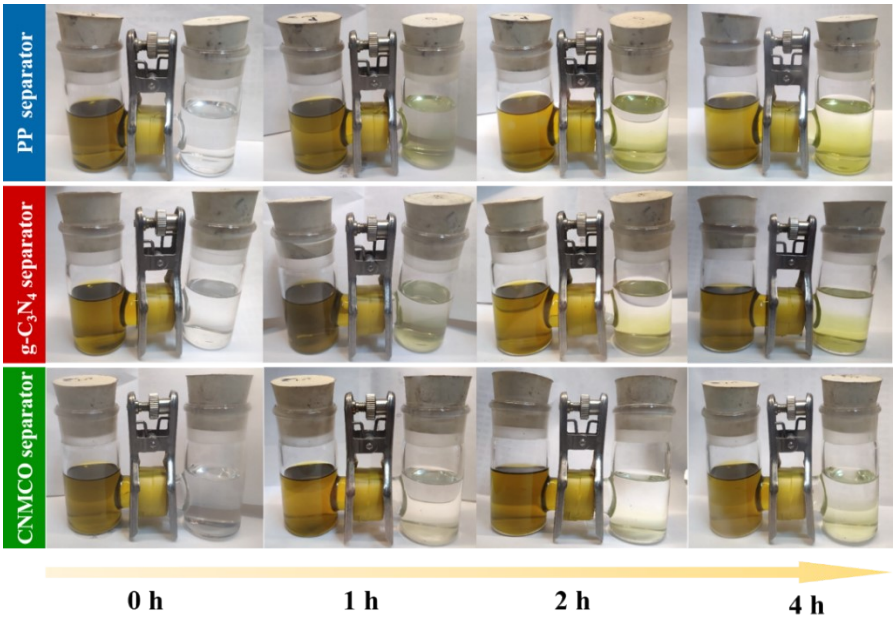

Figure S9. Permeation experiment with the H-type tube for PP separator, g-C_3N_4/PP separator and CNMCO/PP separator.

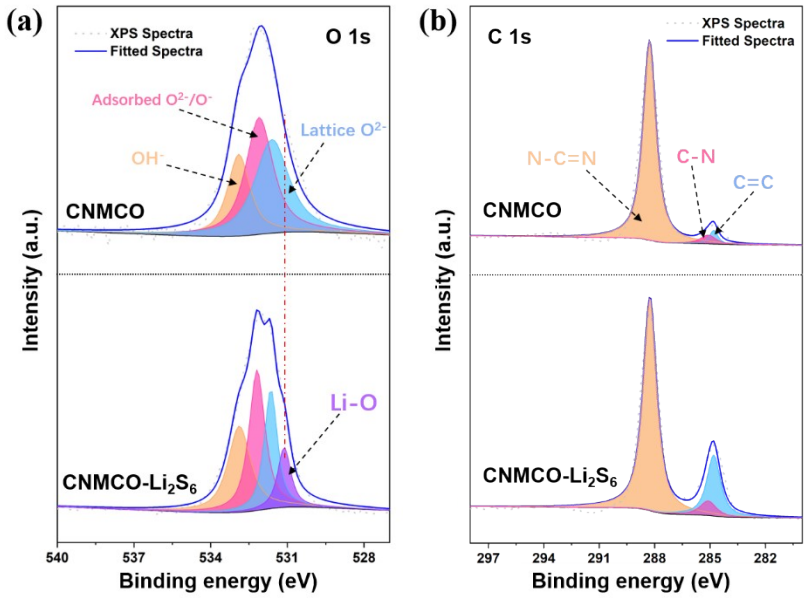

Figure S10. XPS spectra of O 1s and C 1s regions of CNMCO before and after adsorption of Li_2S_6 solution.

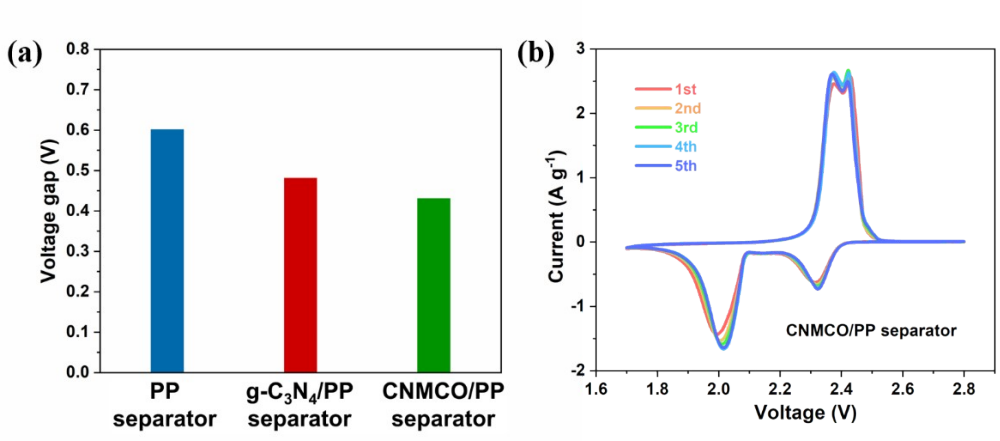

Figure S11. (a) Voltage gaps of cells with different separators. (b) CV curves of the cell with CNMCO/PP separator.

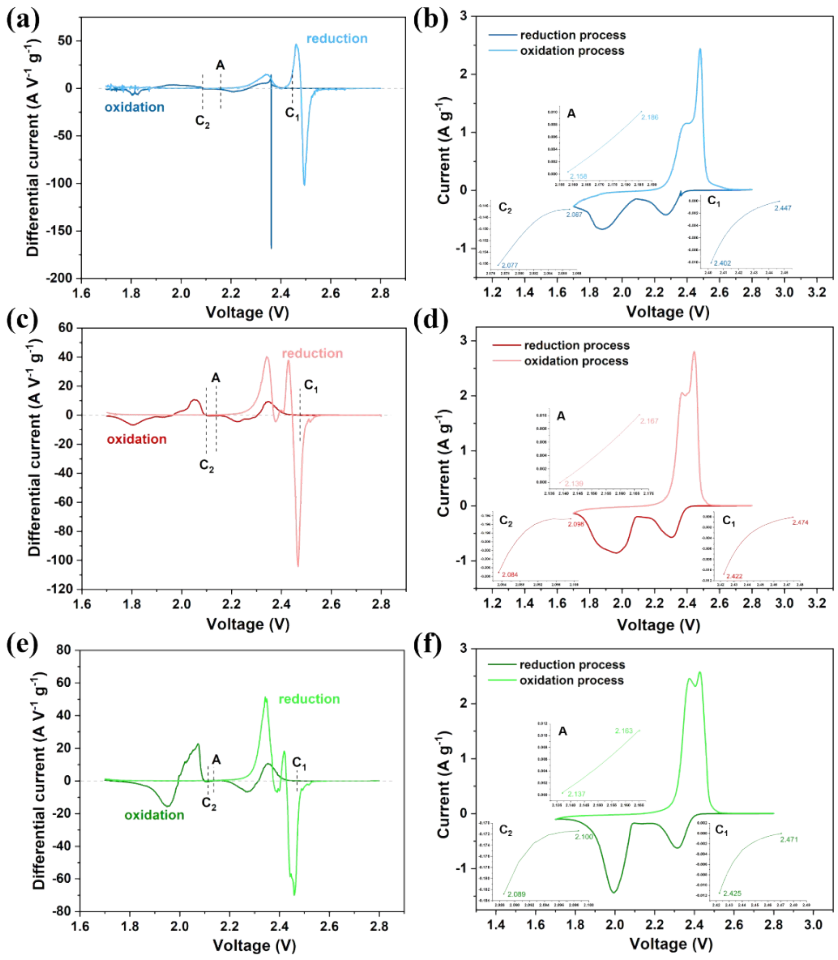

Figure S12. Differential CV curves of cells with (a) PP separator, (c) g-C_3N_4/PP separator and (e) CNMCO/PP separator. CV curves and corresponding onset potentials of redox peaks of cells with (b) PP separator, (d) g-C_3N_4/PP separator and (f) CNMCO/PP separator.

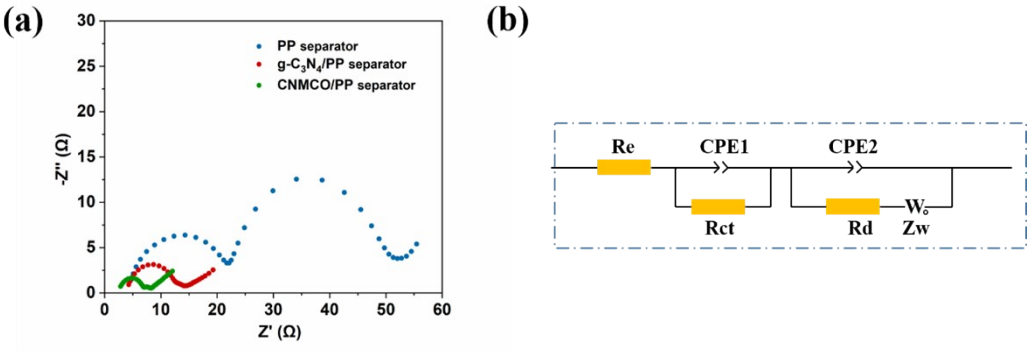

Figure S13. (a) EIS plots of cells with PP, g-C_3N_4/PP, CNMCO/PP separators after cycling. (b) The equivalent circuit models of impedance spectra after cycling.

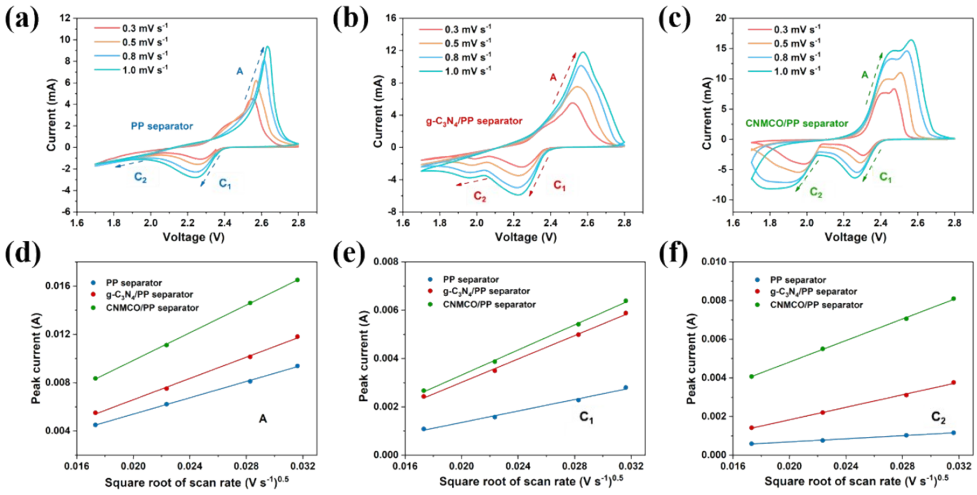

Figure S14. CV curves of cells with (a) PP separator, (b) g-C_3N_4/PP separator and (c) CNMCO/PP separator at various scan rates. Peak currents of (d) anodic oxidation process (Li_2S_2/Li_2S→S_8), (e) first cathodic reduction process (S_8→Li_2S_n, 4≤n≤8), and (f) second cathodic reduction process (Li_2S_n, 4≤n≤8→Li_2S_2/Li_2S) versus the square root of the scan rates.

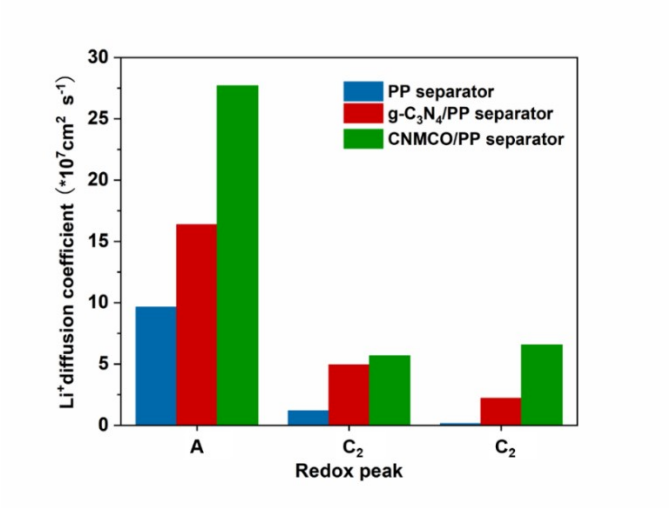

Figure S15. The lithium ion diffusion coefficients of cathodes using PP, g-C_3N_4/PP and CNMCO/PP separators.

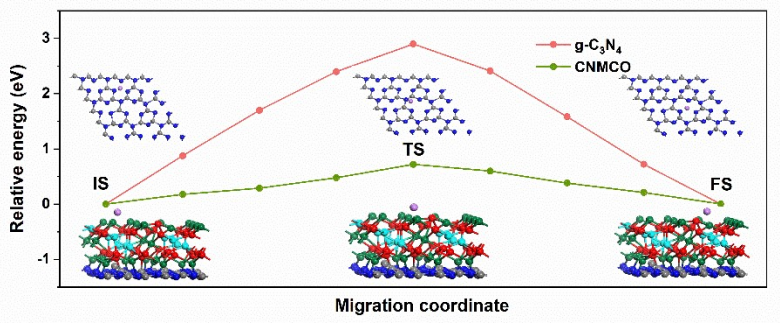

Fig. S16. Diffusion barriers of lithium ion diffusion on g-C_3N_4 and CNMCO and corresponding DFT calculation configurations.

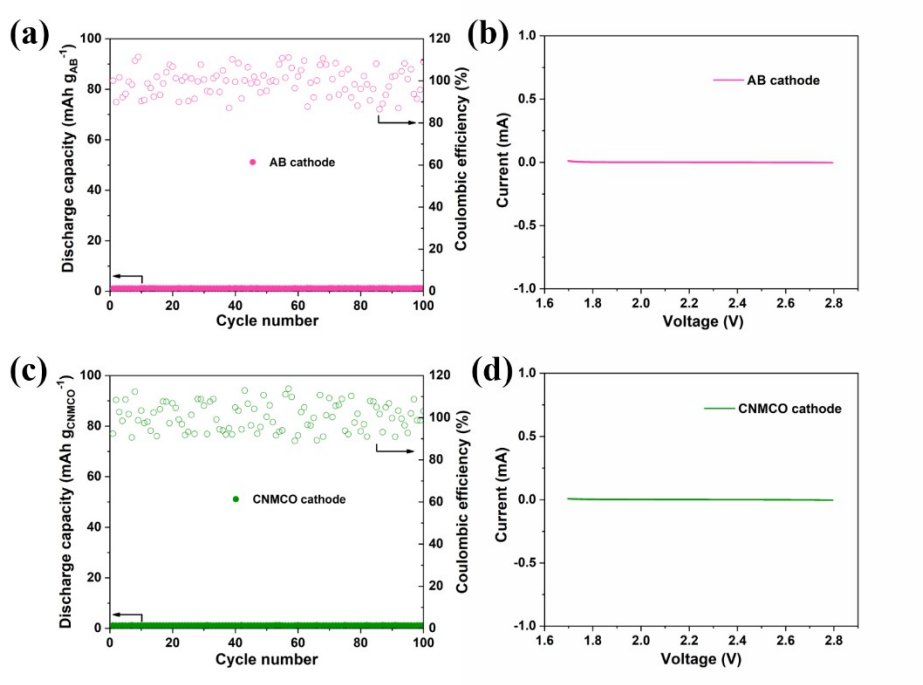

Figure S17. The cycling performances of cells with (a) AB cathode and (c) CNMCO cathode. CV curves of cells with (b) AB cathode and (d) CNMCO cathode.

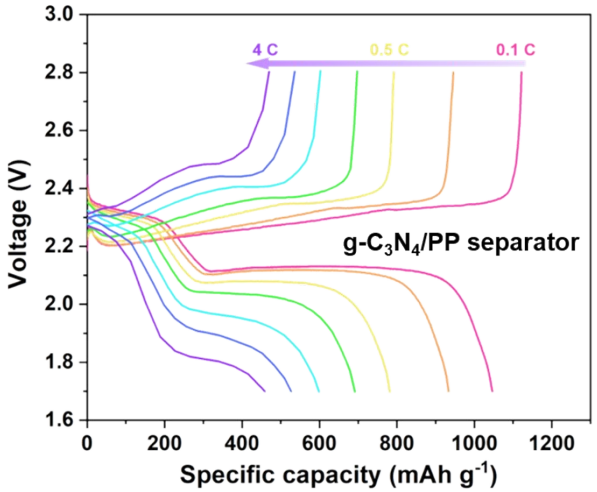

Figure S18. Discharge-charge voltage profiles of cells with g-C_3N_4/PP separator at various rates.

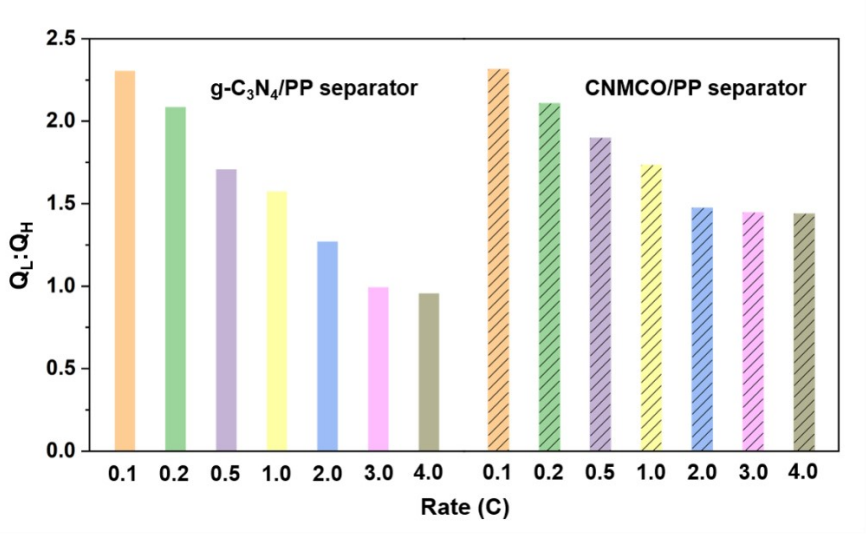

Figure S19. Q_L:Q_H ratios of cells with g-C_3N_4/PP separator and CNMCO/PP separator at different current rates.

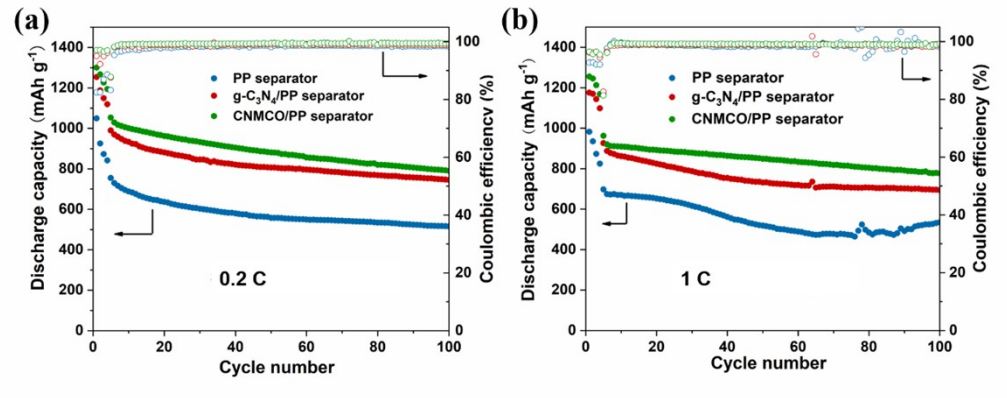

Figure S20. Cycling performances of cells with PP, g-C_3N_4/PP, CNMCO/PP separators at (a) 0.2 C and (b) 1 C.

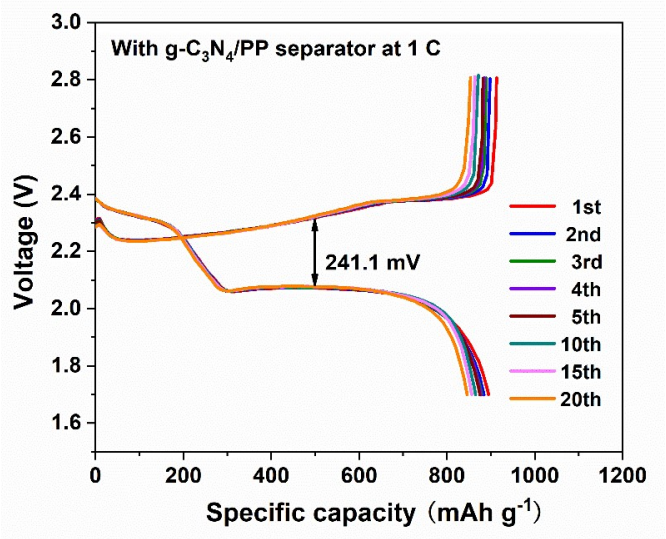

Figure S21. Discharge-charge voltage profiles of the cell with g-C_3N_4/PP separator at 1 C.

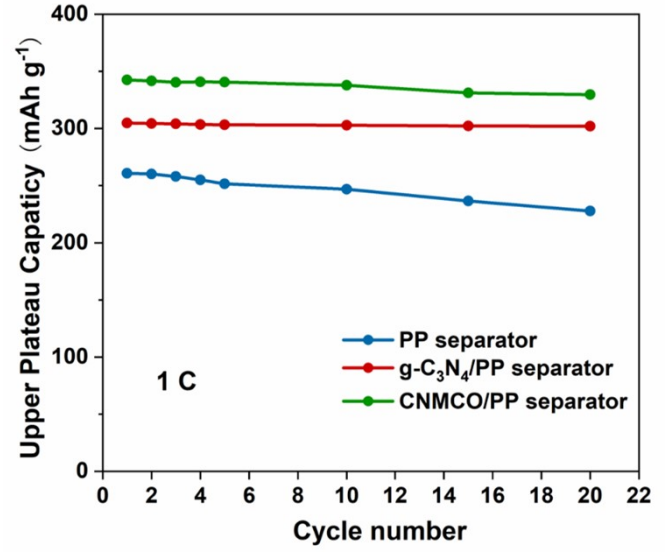

Figure S22. Upper plateau discharge capacity of cells with PP, g-C_3N_4/PP, CNMCO/PP separators at 1 C.

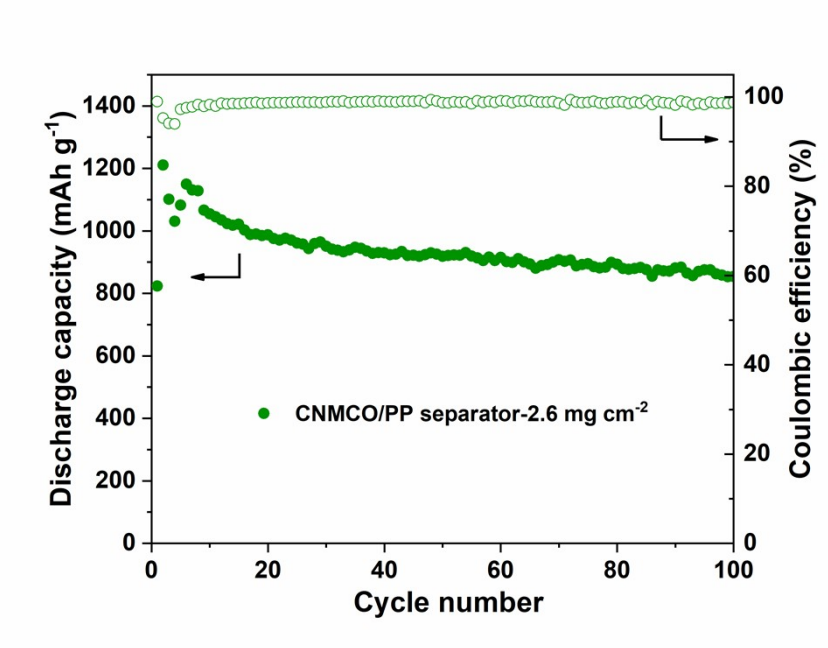

Figure S23. Cycling performance of cell with CNMCO/PP separator using a cathode with sulfur loading of 2.6 mg cm^{-2} at 0.1 C.

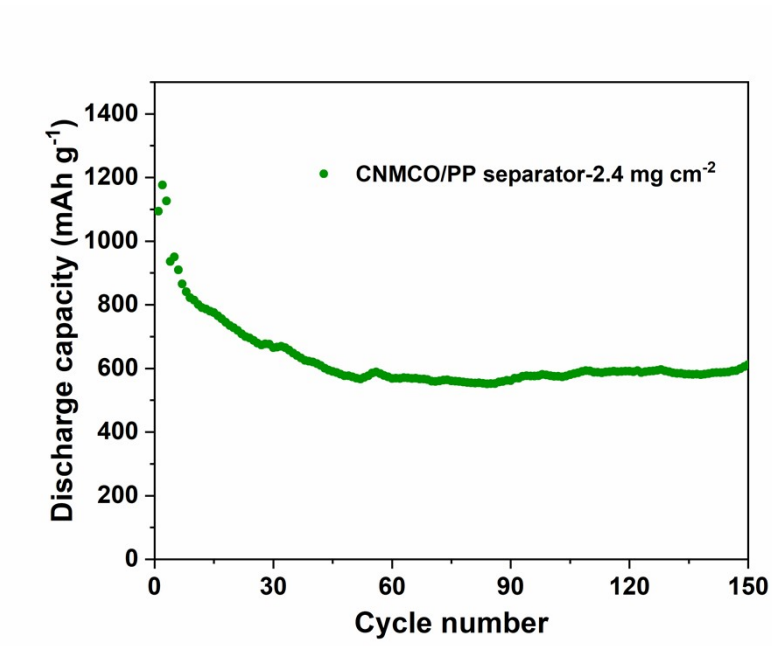

Figure S24. Cycling performance of cell with CNMCO/PP separator using a cathode with sulfur loading of 2.4 mg cm^{-2} at 0.5 C.

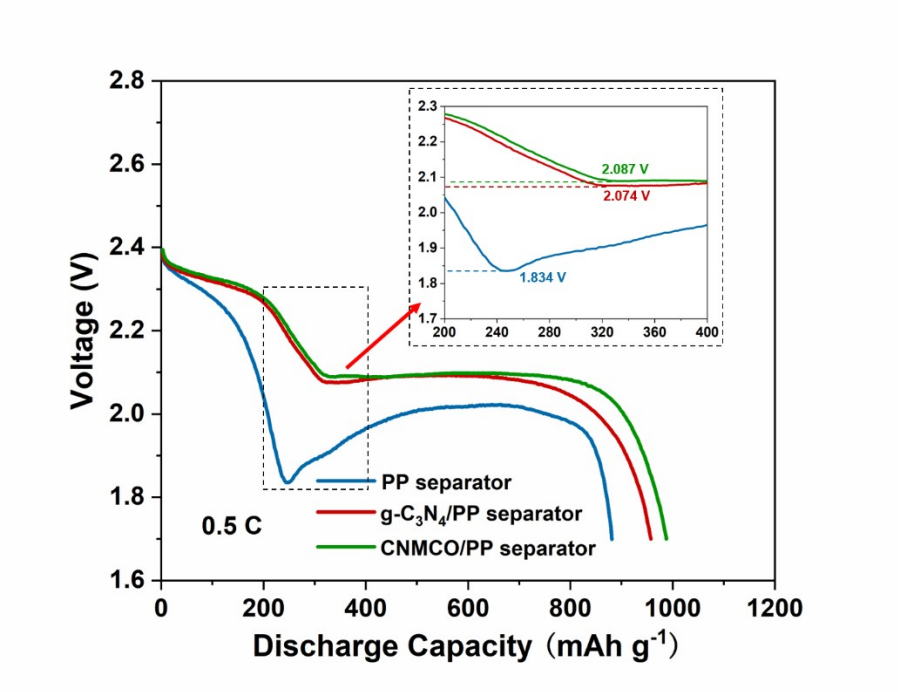

Figure S25. Discharge voltage profiles of cells with PP, g-C_3N_4/PP and CNMCO/PP separators at 0.5 C.

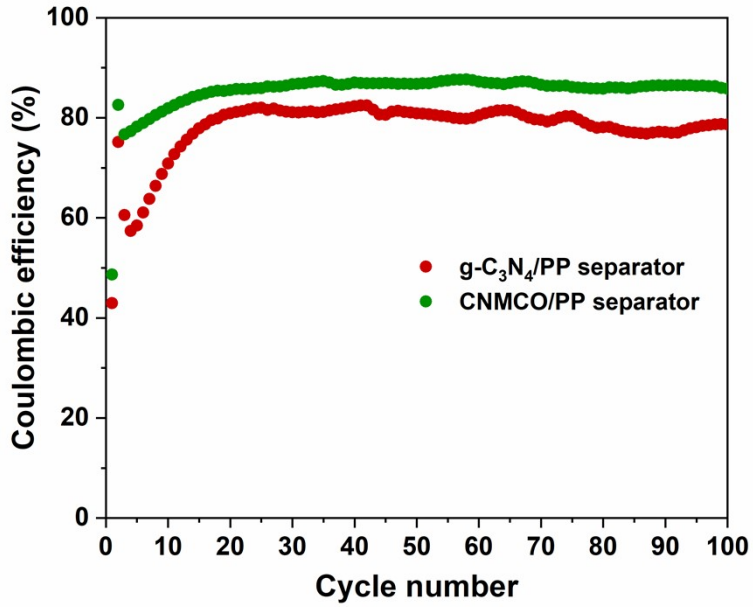

Figure S26. Cycling performances of cells using g-C_3N_4/PP and CNMCO/PP separators at 0.5 C without $LiNO_3$ additive.

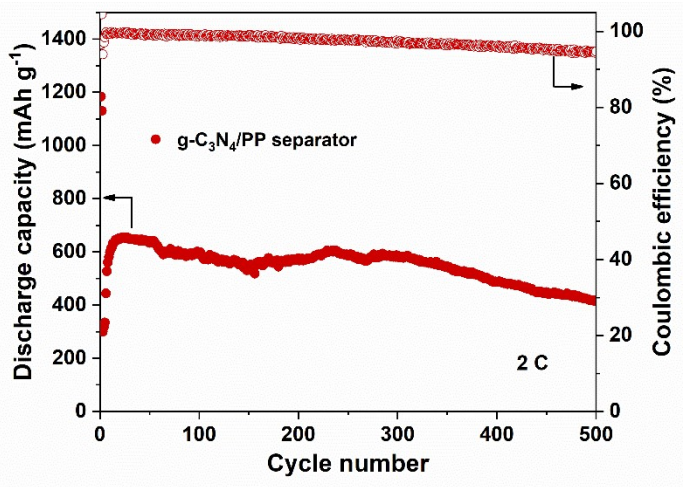

Figure S27. Cycling performance of the cell with g-C_3N_4/PP separator at 2.0 C.

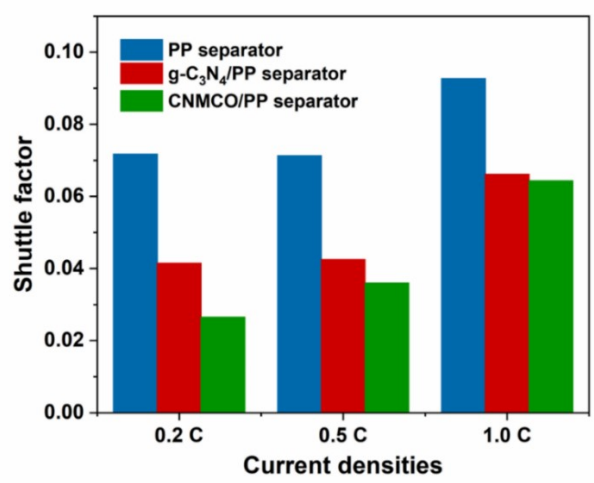

Figure S28. The shuttle factors at different current densities.

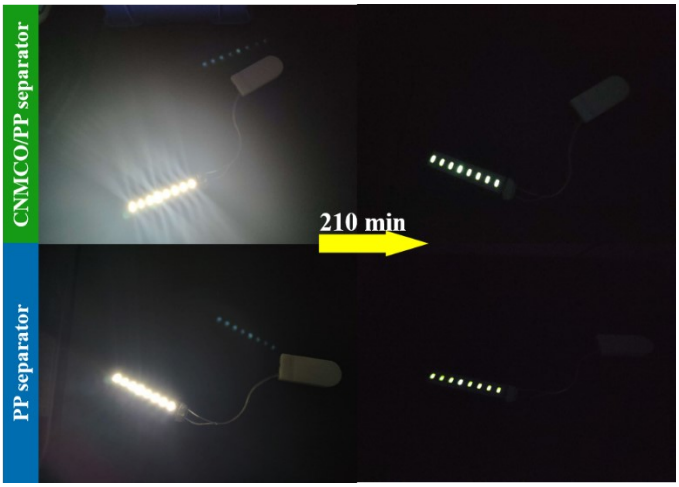

Figure S29. Demonstration of the LED lights powered by the cells with CNMCO/PP separator and PP separator.

Table S1. The onset potentials of cells with different separators.

Cells	Onset potentials (V)		
	C_1:S_8 to Li_2S_n ($4 \le n \le 8$)	C_1: Li_2S_n to Li_2S ($4 \le n \le 8$)	A:Li_2S to Li_2S_n ($4 \le n \le 8$)
with PP separator	2.402	2.077	2.186
with g-C_3N_4 separator	2.422	2.084	2.167
with CNMCO separator	2.425	2.089	2.163

Table S2. EIS results for different separators after cycling.

Cells	R_e (ohm)	R_{ct} (ohm)	R_d (ohm)
with PP separator	4.8	17.1	30.2
with g-C_3N_4 separator	4.3	8.5	1.4
with CNMCO separator	2.9	4.1	1.2

Table S3. Comparison of the electrochemical performance of cells with functional interlayers.

Interlayer type	Reversible discharge capacities at various rates	Ref.
Ti_3C_2 MXene	691, 513 and 403 mAh g^{-1} at 1.0, 2.0 and 4.0 C	1
B/2D MOF-Co	685 and 590 mAh g^{-1} at 1.0 and 2.0 C	2
PAN@ammonium polyphosphate	815, 631 and 507 mAh g^{-1} at 1.0, 2.0 and 3.0 C	3
Co_9S_8	428 mAh g^{-1} at 2.0 C.	4
CNFs	686, 571, 502 and 443 mAh g^{-1} at 1.0, 2.0, 3.0 and 4.0 C	5
H_xMnO_{2+x}/G/CNTs	630 and 515 mAh g^{-1} at 1.0 and 2.0 C	6
C/$Ni_{3-x}ZnC_{0.7}$	638 and 526 mAh g^{-1} at 2.0 and 4.0 C	7
$MnCo_2O_{4.5}$/g-C_3N_4	**744, 652, 650 and 591 at 1.0, 2.0, 3.0 and 4.0 C**	**This work**

(The discharge capacities were obtained from the results in rate performance tests with the sulfur loading of 1-2 mg cm^{-2}.)

Reference

1. Y. Dong, S. Zheng, J. Qin, X. Zhao, H. Shi, X. Wang, J. Chen and Z. S. Wu, *ACS Nano*, 2018, **12**, 2381-2388.
2. Y. Li, S. Lin, D. Wang, T. Gao, J. Song, P. Zhou, Z. Xu, Z. Yang, N. Xiao and S. Guo, *Adv. Mater.*, 2020, **32**, e1906722.
3. T. Lei, W. Chen, Y. Hu, W. Lv, X. Lv, Y. Yan, J. Huang, Y. Jiao, J. Chu, C. Yan, C. Wu, Q. Li, W. He and J. Xiong, *Adv. Energy Mater.*, 2018, **8**, 1802441.
4. J. He, Y. Chen and A. Manthiram, *Energy Environ. Sci.*, 2018, **11**, 2560-2568.
5. S. Karuppiah, B. Kalimuthu, M. A. Nazrulla, S. Krishnamurty and K. Nallathamby, *J. Mater. Chem. A*, 2019, **7**, 10067-10076.
6. Q. Lu, X. Zou, R. Ran, W. Zhou, K. Liao and Z. Shao, *J. Mater. Chem. A*, 2019, **7**, 22463-22474.
7. T. Yang, K. Liu, T. Wu, J. Zhang, X. Zheng, C. Wang and M. Chen, *J. Mater. Chem. A*, 2020, **8**, 18032-18042.